Energy Advances

ROYAL SOCIETY OF CHEMISTRY

PAPER

View Article Online
View Journal | View Issue



Cite this: *Energy Adv.*, 2024, 3, 2648

# Multi-metal (Fe, Cu, and Zn) coordinated hollow porous dodecahedron nanocage catalyst for oxygen reduction in Zn–air batteries†

Yanan Pan,‡[a] Qi Yang,‡[a] Xiaoying Liu,[a] Fan Qiu,[a] Junjie Chen,[a] Mengdie Yang,[a] Yang Fan,[a] Haiou Song[b] and Shupeng Zhang *[a]

Received 8th May 2024,
Accepted 5th September 2024

DOI: 10.1039/d4ya00295d

rsc.li/energy-advances

The coupling of multiple low-cost metals and porous nanocarbon materials aimed at replacing precious metals to enhance electrocatalytic oxygen reduction is a critical challenge in some crucial research areas. In the present study, a hollow dodecahedron nanocage catalyst ($Fe_3O_4$/CuNCs/$ZnN_x$-PHNC) was constructed by supporting copper nanoclusters, $Fe_3O_4$ nanoparticles, and Zn–$N_x$ after sintering and annealing through the coordination of ZIF-8 and by doping copper and iron ions. We observed that the synergy of the multi-metals in the magnetically separable heterojunction catalyst induced electron transfer and inhibited hydrogen peroxide formation, thus improving its catalytic performance for the oxygen-reduction reaction. The catalyst demonstrated a half-wave potential as high as 0.832 V and a Tafel slope of 54 mV decade$^{-1}$, superior to many non-precious metal catalysts reported in the literature. The assembled Zn–air battery (ZAB) exhibited a maximum power density of 162 mW cm$^{-2}$ and ultrahigh stability of >500 h at 5 mA cm$^{-2}$ current density. The ZAB's excellent performance indicates its high development and practical application prospects.



## 1. Introduction

The current global energy shortage has arisen because of the ever-increasing human demand for energy and the associated depletion of available energy resources.[1,2] Human survival, economic status, and sustenance are highly dependent on energy availability, while the exploitation and use of other resources are also energy dependent.[3]

Currently, the rapid development of the electronics industry requires a safe and stable energy supply system.[4] Zn–air batteries (ZABs) are one of the most promising battery candidates because of their high theoretical energy density (1086 W h kg$^{-1}$), low cost, high safety, and environmental friendliness.[5] However, ZABs face some severe setbacks,[6] with the lack of reliable and efficient bifunctional air electrodes as the biggest obstacle to their practical applications.[7] Generally, ZABs' efficiency depends on the catalytic performance of oxygen electrocatalysts on air electrodes, where the discharge process occurs in a kinetically retarded oxygen-reduction reaction (ORR). Therefore, ORR-efficient electrocatalysts are crucial for improving the performance of rechargeable ZABs. Moreover, platinum-based catalysts are typical commercial electrocatalysts for the ORR with excellent activity. However, their high cost, the natural scarcity of platinum, and their unsatisfactory durability limit their large-scale industrial applications.[8,9] Therefore, there is an urgent need to develop highly active, durable, and cost-effective ORR catalysts.

Transition metals and their derivatives (bearing aluminum, oxygen, nitrogen, sulfur, selenium, carbides and hydroxides and their corresponding oxides, nitrides, sulfides, *etc.*) have attracted huge interest owing to their earth-abundance and high catalytic properties.[10–13] Among them, Fe- and Cu-based nanoparticles are of immense interest because of their high electrical conductivity, excellent mechanical strength, and flexible electronic structure.[14–16] However, finding a suitable catalyst substrate to load active nanoparticles is essential to expose the active sites more entirely for improved activity.

Zeolitic imidazolate frameworks (ZIFs) constructed from coordination networks between specific metal nodes and organic ligands are attractive substrates considering their unique properties of a high specific surface area, large pore volume, and multiple organometallic nature.[17] Given these properties, ZIF-based materials have been widely applied in adsorption and purification.[18] Introducing metallic species into ZIF precursors can inhibit the aggregation of nanoparticles

[a] *School of Chemistry and Chemical Engineering, Nanjing University of Science and Technology, Nanjing, 210094, PR China. E-mail: shupeng_2006@126.com; Fax: +86 25 84315519; Tel: +86 25 84315519*
[b] *School of Environment, Nanjing Normal University, Nanjing, 210097, PR China*

† Electronic supplementary information (ESI) available. See DOI: https://doi.org/10.1039/d4ya00295d

‡ Y. N. Pan and Q. Yang contributed equally to this work.

using a strong anchoring effect, thereby leading to highly dispersed active sites. Additionally, calcination at high temperatures ensures a high graphitization of carbon precursors, which can improve the corrosion resistance and electrical conductivity.[19] Due to their relatively high activity, Fe-doped ZIF materials are considered among the most promising oxygen-reduction electrocatalysts to replace the noble metal Pt.[20–22] However, the $H_2O_2$ produced by the Fe–N–C catalyst formed by single-metal Fe doping in the ORR severely hinders the four-electron-transfer process in the ORR. As a result, the Fe active sites easily undergo the Fenton reaction with $H_2O_2$, potentially affecting the ORR activity.[23,24]

To overcome this drawback, other metals can be doped to induce electron transfer and inhibit $H_2O_2$ production. The significant synergistic effect between $Fe_3O_4$ nanoparticles and Cu nanoclusters' catalytic active sites and carbon carriers effectively improves the electrocatalytic activity.[25,26] In addition, Zn has less electronegativity ($c$ = 1.65), making it easier to contribute its most valent electrons to Cu ($c$ = 1.90) and Fe ($c$ = 1.83). Therefore, Zn is compatible with Cu and Fe, and can optimize the electronic structure to produce synergy, promote the adsorption of reaction molecules and desorption of reaction intermediate, and improve the catalytic performance.[27] Therefore, in the present study we employed ZIF-8 with a Zn atom as the substrate and introduced Fe and Cu atoms to construct composite catalysts.

The high surface area and short diffusion path of hollow nanocages provide more active sites, a larger liquid–solid contact area, and a relatively large functional surface for the adsorption–desorption of the substrate molecules themselves to promote the adsorption–desorption rate.[28,29] Meanwhile, the hollow interior can prevent the encapsulated transition metal oxide nanoparticles from aggregating. The high dispersion of metal nanoparticles on the carbon skeleton can expose more active sites, providing excellent electrical conductivity and allowing for fast mass transfer. In addition, anisotropic nanocages have the characteristics of a uniform size, low density, large void space, and strong shell permeability, *etc.*, which have strong utilization value for electrocatalysis.[30] The synergetic enhancement of the interface structure and active sites on the catalyst utilizes the inherent advantages of the interface structure.[31] Therefore, distributing the various nanoparticles entirely on the graded porous carbon and leveraging their synergistic advantages to promote catalytic performance has become a major challenge. Therefore, it is imperative to develop a transition metal-regulated skeletonization gold nanocage structure with a controllable microstructure to reveal changes in the electronic and environmental properties at the coupling interface, clarify the structural performance of the synergistic effect, and improve the ORR performance.[32]

The current research prepared a hollow-graded, porous carbon-based, cage-like catalyst co-regulated by multiple metals, and successfully applied it to ORR reactions and zinc–air batteries. We used ZIF-8 containing zinc, nitrogen, carbon, and oxygen as the precursor, which was transformable into a material with porous carbon-containing Zn–$N_x$ active sites after high-temperature pyrolysis. Fe and Cu ions were introduced through coordination during ZIF-8 synthesis, and high-temperature sintering synchronously generated a hollow carbon-based catalyst controlled by the multiple metals. Further, salt melting and high-temperature annealing resulted in pore formation, and a hollow-graded porous carbon-based catalyst (named $Fe_3O_4$/CuNCs/Zn$N_x$-PHNC) was obtained. The magnetically separable catalyst had a high specific surface area and high metal loading capacity. Moreover, $Fe_3O_4$, composed of Fe species with various valence states, could provide active sites for electron acquisition and loss, ensuring a high ORR activity. Second, the Cu nanoclusters have excellent stability, conductivity, and abundant oxygen defects, which can accelerate the conductivity of O-containing intermediates, thereby extending the lifespan of the $Fe_3O_4$/CuNCs/Zn$N_x$-PHNC catalysts.

This study provides an effective strategy for synthesizing non-noble metal catalysts for use in ZABs. The assembled ZABs and flexible zinc–air batteries (FZABs) exhibited excellent discharge performances and strong stability, reflecting their optimistic commercial prospects and application value as air cathode catalysts.

## 2. Experimental section

### 2.1 Synthesis of ZIF-8

The production method for ZIF-8 refers followed the literature with some improvements.[33,34] First, zinc nitrate hexahydrate (1.16 g) and dimethylimidazole (2.46 g) were dissolved in 40 ml of methanol, sonicated for 10 min, mixed and stirred for 12 h, and then rested at room temperature for 12 h. The supernatant after resting was poured out, then washed three times each with ultrapure water and ethanol, and dried in a vacuum oven at 60 °C to obtain ZIF-8 white crystals.

### 2.2 Synthesis of Fe-ZIF-8 and Cu-ZIF-8

Following the same procedure used for the synthesis of ZIF-8, zinc nitrate hexahydrate (1.16 g) and iron acetylacetonate (0.35 g) were dissolved in 40 ml of methanol, and dimethylimidazole (2.46 g) was dissolved in 40 ml of methanol, sonicated for 10 min, mixed and stirred for 12 h, and then rested at room temperature for 12 h. The supernatant after resting was poured out, then washed three times each with ultrapure water and ethanol, and dried in a vacuum oven at 60 °C and the final product was named Fe-ZIF-8. The synthesis process was the same as for Fe-ZIF-8 except that iron acetylacetonate was replaced by copper nitrate (0.1 g), and the resulting product was named Cu-ZIF-8.

### 2.3 Synthesis of Fe/Cu-ZIF-8

Iron acetylacetonate (0.35 g), copper nitrate (0.1 g), and zinc nitrate hexahydrate (1.16 g) were dissolved simultaneously in 40 ml of methanol, and the subsequent treatment was the same as that for the synthesis of ZIF-8.

### 2.4 Synthesis of $Fe_3O_4$/CuNCs/Zn$N_x$-PHNC

The dried product was mixed with NaCl and KCl (1 : 4 : 1). After sintering at 925 °C for 2 h, the calcined products of ZIF-8,

Cu-ZIF-8, Fe-ZIF-8, and Fe/Cu-ZIF-8 were extracted and filtered. The final catalysts were named $ZnN_x$-PNC, CuNCs/$ZnN_x$-PNC, $Fe_3O_4$/$ZnN_x$-PHNC, and $Fe_3O_4$/CuNCs/$ZnN_x$-PHNC. For the convenience of readers, we list the raw materials and the corresponding obtained materials in Table S1 (ESI†).

## 3. Results and discussion

### 3.1. Structure and characterization of the catalysts

The preparation procedure of $Fe_3O_4$/CuNCs/$ZnN_x$-PHNC is shown in Fig. 1a. To synthesize Fe–Cu-ZIF-8, the precursors were first synthesized by dissolving a mixture of iron acetylacetonate, copper nitrate, and zinc nitrate hexahydrate in methanol before introducing imidazole dialdehyde dissolved in methanol with stirring at room temperature. Calcining $Fe_3O_4$/CuNCs/$ZnN_x$-PHNC in the presence of NaCl and KCl under an Ar atmosphere formed the hollow-structured $Fe_3O_4$/CuNCs/$ZnN_x$-PHNC.

Metal doping was determined from the X-ray diffraction (XRD) images of all the materials before sintering. As shown in Fig. S1 (ESI†), all the synthesized precursors conformed with the theoretical ZIF-8 peak structure. However, spurious peaks appeared at individual locations, attributable to the metal doping. Fig. 2a shows the XRD diffraction images of the four materials after sintering. The graphitic structure formed after calcination evinced the (002) diffraction peak centered at 25.4° and the (101) diffraction peak at 43.2° as the major crystallographic planes of C. For $Fe_3O_4$/CuNCs/$ZnN_x$-PHNC, the 19.7° and 43.1° spikes corresponded to the crystallographic planes (212) and (440) of $Fe_3O_4$ (PDF#76-0956), respectively. Combined with the standard PDF card for Cu (PDF#04-0836), peaks for the Cu nanoclusters were also evident in the XRD pattern of $Fe_3O_4$/CuNCs/$ZnN_x$-PHNC. The uniform embedding of Cu nanoclusters in the carbon layer as active sites is crucial for promoting the ORR performance. The XRD pattern of $Fe_3O_4$/$ZnN_x$-PHNC only showed a weak $Fe_3O_4$ characteristic peak at 15.3°, likely due to the lack of Cu regulation and the minute $Fe_3O_4$ produced, mainly responsible for the lack of expected catalytic effect. Also, the XRD pattern of CuNCs/$ZnN_x$-PNC did not show any Cu peak, indicating that single-metal doping could not stably form metal nanoclusters. In addition, only carbon peaks were observed in $ZnN_x$-PNC.

The hysteresis curve (VSM) represents the magnetization of a ferromagnetic substance under alternating external magnetic

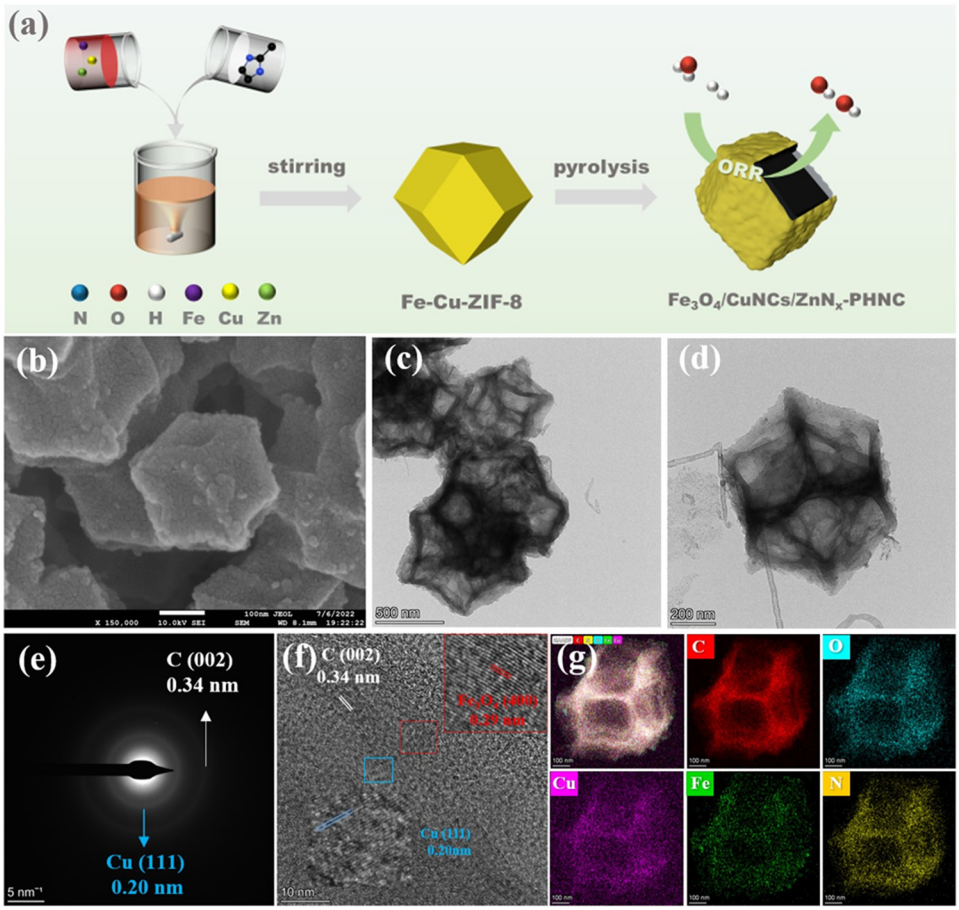


Fig. 1 (a) Flow chart for the preparation of $Fe_3O_4$/CuNCs/$ZnN_x$-PHNC; (b) SEM images of $Fe_3O_4$/CuNCs/$ZnN_x$-PHNC at different resolutions; (c) and (d) TEM images of $Fe_3O_4$/CuNCs/$ZnN_x$-PHNC at different resolutions; (e) selected area electron diffraction images of $Fe_3O_4$/CuNCs/$ZnN_x$-PHNC; (f) high-resolution TEM images of $Fe_3O_4$/CuNCs/$ZnN_x$-PHNC; (g) HAADF-STEM images of $Fe_3O_4$/CuNCs/$ZnN_x$-PHNC and its elemental distribution images.

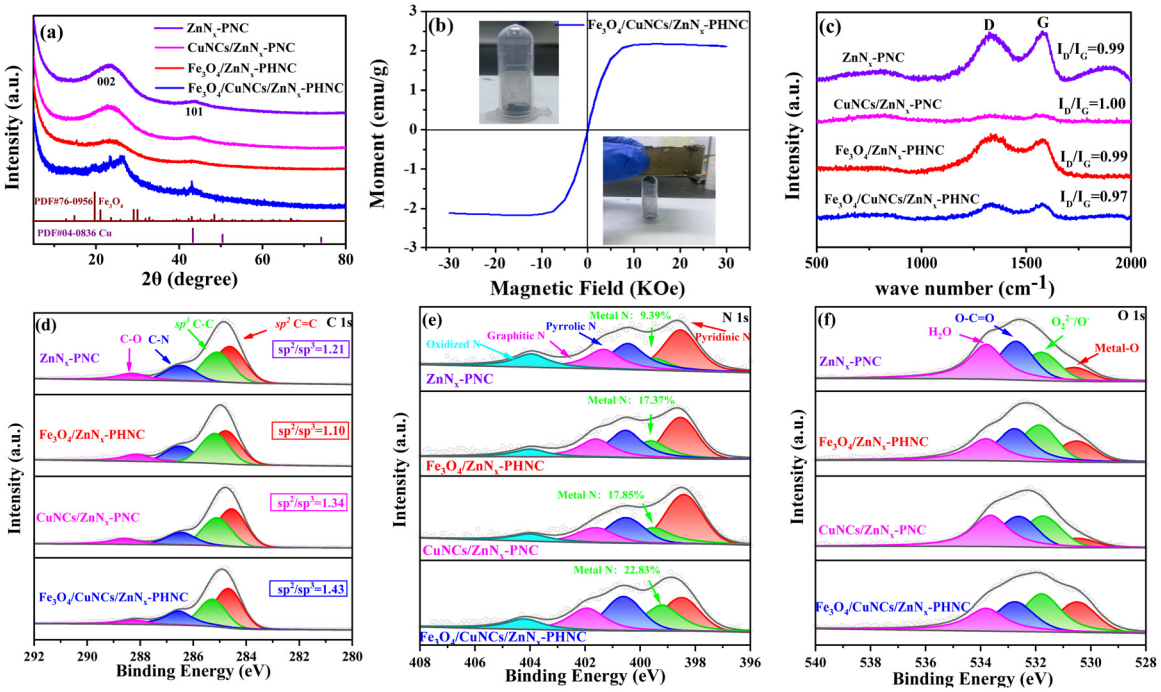


Fig. 2 (a) XRD spectra of $Fe_3O_4$/CuNCs/$ZnN_x$-PHNC, $Fe_3O_4$/$ZnN_x$-PHNC, CuNCs/$ZnN_x$-PNC and $ZnN_x$-PNC; (b) VSM curves of $Fe_3O_4$/CuNCs/$ZnN_x$-PHNC; (c) Raman spectra of $Fe_3O_4$/CuNCs/$ZnN_x$-PHNC, $Fe_3O_4$/$ZnN_x$-PHNC, CuNCs/$ZnN_x$-PNC and $ZnN_x$-PNC; (d) C 1s, (e) N 1s and (f) O 1s XPS spectra of $Fe_3O_4$/CuNCs/$ZnN_x$-PHNC, $Fe_3O_4$/$ZnN_x$-PHNC, CuNCs/$ZnN_x$-PNC and $ZnN_x$-PNC.

field strengths. When the magnetization starts (Fig. 2b), the magnetic induction strength of the ferromagnet increases with the external magnetic field strength and the unit moment. At a certain magnetic field strength, the magnetic induction strength of the ferromagnet is optimized, and the unit moment plateaus. The inset shows the $Fe_3O_4$/CuNCs/$ZnN_x$-PHNC catalyst powder, which was suspended when magnetized, indicating its strong magnetic property. This observation was consistent with the peak structure of $Fe_3O_4$ nanoparticles from the XRD spectra.

To investigate the structural defects and the degree of graphitization in the carbon materials, the Raman spectra of $Fe_3O_4$/CuNCs/$ZnN_x$-PHNC, $Fe_3O_4$/$ZnN_x$-PHNC, CuNCs/$ZnN_x$-PNC, and $ZnN_x$-PNC were examined (Fig. 2c). The D-band (1350 $cm^{-1}$) was the vibration caused by lattice defects in the carbon matrix, corresponding to the defect position of $sp^3$, while the G-band (1580 $cm^{-1}$) was caused by vibrations belonging to the $sp^2$ bonded graphitic carbon. The samples' intensity ratios ($I_D/I_G$) of the D-band to G-band were 0.97, 0.99, 1.00, and 0.99, respectively. The intensity ratio for $Fe_3O_4$/CuNCs/$ZnN_x$-PHNC was 0.97, indicating the presence of many defects in the carbon matrix. These defects in the lattice are essential sites for enhancing the electrocatalytic performance of the catalyst.[35] Comparing the other three materials, we observed that the materials showed a large number of carbon defects and increased graphitization when calcined with added protective and stripping agents. This result shows that sintering and activators are crucial for preparing nanocarbon materials.[36,37]

$N_2$ adsorption–desorption experiments were performed to further investigate the pore structures and specific surface areas of $Fe_3O_4$/CuNCs/$ZnN_x$-PHNC, $Fe_3O_4$/$ZnN_x$-PHNC, CuNCs/$ZnN_x$-PNC, and $ZnN_x$-PNC. The adsorption isotherms (Fig. S2a, ESI†) illustrated that the materials were characterized by hysteresis-return type IV profiles. Also, the samples had high specific surface areas and extensive porosity. From Fig. S2b (ESI†), the specific surface areas of $Fe_3O_4$/CuNCs/$ZnN_x$-PHNC, $Fe_3O_4$/$ZnN_x$-PHNC, CuNCs/$ZnN_x$-PNC, and $ZnN_x$-PNC were derived as 702, 773, 853, and 894 $m^2\ g^{-1}$, respectively. Their pore size distribution (Fig. S2c, ESI†) was mainly dominated by micropores and mesopores, in which the hierarchical porous structure can shorten the distance for $O_2$, thus accelerating the electron transport and mass transfer.[38] Table S2 (ESI†) suggests that introducing Fe and Cu decreased the microporosity of $Fe_3O_4$/CuNCs/$ZnN_x$-PHNC, whereas the average pore size (calculated by BJH) was the largest. This was related to the fact that the total BET, micropore area, and pore capacity ratio were reduced correspondingly with the magnitude of metal doping. CuNCs/$ZnN_x$-PNC and $ZnN_x$-PNC showed some folds spreading and may also exfoliate some graphitized lamellae, thus significantly altering their pore structure.

Furthermore, X-ray photoelectron spectroscopy (XPS) was used to assess the elemental composition of the catalysts. The samples' surface elemental contents are listed in Table S3 (ESI†). Fig. S3a (ESI†) illustrates the full spectra of $Fe_3O_4$/CuNCs/$ZnN_x$-PHNC, $Fe_3O_4$/$ZnN_x$-PHNC, CuNCs/$ZnN_x$-PNC, and $ZnN_x$-PNC, showing the peaks of the elements in the various speciations. From the high-resolution spectrum of C 1s (Fig. 2d), the C peaks could be divided into four peaks: 284.7 ± 0.1, 285.2 ± 0.1, 286.5 ± 0.1, and 288.4 ± 0.2 eV, corresponding to C=C, C–C, C–N, and C–O bonds, respectively. Among these, the C–N bond indicated the successful doping of N atoms into the carbon nanostructures.

The main peak at 284.7 ± 0.1 eV was ascribed to $sp^2$ hybridized carbon, while that at 285.2 ± 0.1 eV belonged to $sp^3$ hybridized carbon. The $sp^2$ hybridized carbon significantly improves the conductivity of materials.[39] Conversely, the conductivity and catalytic activity of $sp^3$-hybridized carbon are relatively low.[40]

Here, we compared the corresponding peak areas of the three metal-doped materials with the total peak area of C 1s (Table S4, ESI†) and calculated the relative contents of $sp^2$ and $sp^3$ based on the area ratio. The $sp^2/sp^3$ ratio values of $ZnN_x$-PNC, $Fe_3O_4/ZnN_x$-PHNC, CuNCs/$ZnN_x$-PNC, and $Fe_3O_4$/CuNCs/$ZnN_x$-PHNC were 1.21, 1.10, 1.34, and 1.43, respectively. $Fe_3O_4$/CuNCs/$ZnN_x$-PHNC's surface has a relatively high $sp^2$ hybrid carbon content and corresponding high electrical conductivity. The N 1s spectrum could be deconvoluted into peaks located at 398.5 ± 0.1, 399.4 ± 0.2, 400.5 ± 0.1, 401.6 ± 0.3, and 404.0 eV, ascribed to pyridinic nitrogen, metal–N, pyrrolic nitrogen, graphitic nitrogen, and nitrogen oxide species, respectively (Fig. 2e). The metal–N bonding pattern indicated that metals and N combined to form metal–N active sites between the carbon skeleton, contributing significantly to the ORR activity enhancement. By calculating the ratio of each peak area to the total peak area, the metal–N active site content was obtained (Table S5, ESI†). The metal–N content of $Fe_3O_4$/CuNCs/$ZnN_x$-PHNC was 22.83%, evincing the sample's best ORR performance.

The XPS high-resolution spectra of O 1s exhibited main peaks at 530.5 ± 0.1, 531.8 ± 0.1, 532.7 ± 0.1, and 533.7 ± 0.1 eV, corresponding to metal–O, $O_2^{2-}/O^-$, C–C═O, and $H_2O$, respectively (Fig. 2f). $O_2^{2-}/O^-$ is the chemisorbed oxygen, which is closely related to oxygen vacancies. Oxygen vacancies are crucial in regulating the surface electronic state, accelerating the oxygen-containing intermediate transfer, and enhancing the interaction between transition metal nanoparticles and carbon carriers; thus, enriching the electrochemical activity and enhancing the catalyst stability.[41] Based on the ratio of the corresponding peak area to the total peak area, we could deduce the oxygen-vacancy content in the different substances. According to the peak proportion of the metal-doped materials (Table S6, ESI†), $Fe_3O_4$/CuNCs/$ZnN_x$-PHNC had the highest surface oxygen-vacancy content, accounting for 33.75% of the total area. The XPS high-resolution spectrum of Fe 2p showed that Fe was primarily present as $Fe^{2+}$ and $Fe^{3+}$, as evidenced by the Fe $2p_{1/2}$ and Fe $2p_{3/2}$ orbital peaks, respectively. The peaks could be further deconvoluted into four peaks (Fig. S3b, ESI†),[42] whereby the two peaks at 711.0 ± 0.2 and 712.8 ± 0.1 eV corresponded to the Fe $2p_{3/2}$ orbital, while the two peaks at 724.2 ± 0.2 and 726.0 ± 0.1 eV were designated as Fe $2p_{1/2}$ spin–orbit peaks. The absence of satellite peaks also corroborated the assignment of the final product to $Fe_3O_4$ rather than $Fe_2O_3$.[43,44]

Furthermore, the XPS high-resolution spectra of Cu 2p were dominated by Cu at peak positions of 934.1 ± 0.4 and 955.0 ± 0.6 eV, with Cu $2p_{3/2}$ and Cu $2p_{1/2}$ present (Fig. S3c, ESI†). These were consistent with the XPS images of Cu 2p in copper nanoclusters documented in other literature.[45] In the XPS spectra of Zn 2p (Fig. S3d, ESI†), peaks were observed at 1021.9 ± 0.1 and 1045.2 ± 0.2 eV, corresponding to $Zn^{2+}$.[46] Because the boiling point of zinc is 907 °C, many experiments ignore Zn's presence after high-temperature calcination. However, while most zinc particles evaporate to form defects, the remaining atoms form Zn–N bonds, preventing them from evaporating.[47] This result was also consistent with that found with metal–N bonds in the N 1s map of $ZnN_x$-PNC, which was without transition metal doping.

The content ratio of metals in the materials was estimated using inductively coupled plasma mass spectrometry (ICP-MS). The concentrations of Fe, Cu, and Zn in the final product were 179.08, 17.06, and 10.80 ppb, respectively, with corresponding content ratios of 3.6%, 0.34%, and 0.21%.

The morphology and composition of the materials' surface ultrastructures were examined by scanning electron microscopy (SEM). From the SEM image of the Fe/Cu-ZIF-8 precursor (Fig. S4a–c, ESI†), we observed that the ZIF-8 surface was wrinkled by Fe and Cu. However, the SEM micrographs of Fe-ZIF-8 (Fig. S4d–f, ESI†) and Cu-ZIF-8 (Fig. S4g–i, ESI†) showed no significant changes in morphology, indicating that single-metal doping did not significantly alter the dodecahedral structure of ZIF-8 when the precursor was synthesized. To further describe the basic three-dimensional and surface microscopic morphologies of the materials, we studied the SEM images of the materials after calcination. Fig. 1b and Fig. S5a–c (ESI†) show that $Fe_3O_4$/CuNCs/$ZnN_x$-PHNC retained a complete dodecahedral structure, presenting some grain-like substances on the surface, preliminarily assumed as nanoparticles and nanoclusters formed by the metals. After calcination, the degree of graphitization and carbon defects of the material were significantly increased, which are crucial to increasing the conductivity and catalytic activity of the material. The basic morphology maintained by $Fe_3O_4/ZnN_x$-PHNC (Fig. S5d–f, ESI†) was similar to that of $Fe_3O_4$/CuNCs/$ZnN_x$-PHNC. However, the CuNCs/$ZnN_x$-PNC surface (viewed at various resolutions) was smooth (Fig. S5g–i, ESI†), and wrinkled nanosheets appeared on the surface in the presence of activators and stripping agents. SEM proved that Fe contributes significantly to inducing the hollow nanocages. The SEM image of $ZnN_x$-PNC (Fig. S5j–l, ESI†) confirmed that without metal doping, the complete dodecahedral structure could no longer be retained after high-temperature calcination, also proving that transition metal doping was essential to the structural stability of the material.

Further morphological observations were done using transmission electron microscopy (TEM). Fig. 1c depicts the TEM images of $Fe_3O_4$/CuNCs/$ZnN_x$-PHNC at 500 nm resolution, showing that the sintered ZIF-8 did not agglomerate, retaining the dodecahedral structure.[48] Fig. 1d shows that the $Fe_3O_4$/CuNCs/$ZnN_x$-PHNC dodecahedra had a laminar wrinkled nanosheet structure in the outer layer and distinct skeletonization in the inner layer, showing several dispersed skeletonized nanocage structures overall. The large number of defects formed in the outer and inner layers after calcination provided abundant electron-transport channels that enhanced $O_2$ adsorption and shortened the mass-transfer distance, which were primarily responsible for the enhanced activity of

 

$Fe_3O_4$/CuNCs/$ZnN_x$-PHNC.[49] Fig. S6a–c (ESI†) show the TEM images of $Fe_3O_4$/$ZnN_x$-PHNC at different resolutions. The sample maintained the basic dodecahedral structure, with folded nanosheets on the outer layer and skeletonized porous layers on the inner layer. These structural forms were similar to those of $Fe_3O_4$/CuNCs/$ZnN_x$-PHNC. In contrast, CuNCs/$ZnN_x$-PNC (Fig. S6d–f, ESI†) showed no skeletonization despite the folded nanosheets on the surface, consistent with the SEM imagery. Moreover, $ZnN_x$-PNC (representing the undoped transition metal) showed an irregular nanobulk after calcination (Fig. S6g–i, ESI†), with a rough surface and no skeletalization. This indicated that the basic skeleton of the material was destroyed by the high-temperature calcination *via* its collapse and splitting. The analysis showed that the Fe-doped carbon precursor could form skeletonized nanocages during calcination, while the non-doped metal precursor could not maintain a complete dodecahedral structure after sintering. The reason may be that in the early stages of calcination, $Fe^{3+}$ forms an oxide of Fe on the surface of ZIF-8, and as calcination continues, the Kirkendall effect occurs between $Zn^{2+}$ and the oxide of Fe to form ZnO. The continuous inhomogeneous interdiffusion of $O^{2-}$ ions and $Zn^{2+}$ ions on ZIF-8 leads to the emergence of Kirkendall holes.[50] The loss of $Zn^{2+}$ destroys the crystal structure of ZIF-8, and the organic ligand dimethylimidazole evaporates from the interior due to the lack of coordination, causing ZIF-8 to gradually become hollow.[51] Thus, metal doping is crucial for stabilizing the transition material morphology during calcination.

The selected electron diffraction (SAED) pattern of $Fe_3O_4$/CuNCs/$ZnN_x$-PHNC (Fig. 1e) showed two diffracted circles. The radii of the outermost and innermost circles were 0.34 and 0.20 nm, respectively, corresponding to the (002) crystal plane of C and (111) crystal plane of Cu nanoclusters.[52] Fig. 1f depicts a high-resolution transmission electron microscopy (HRTEM) image of $Fe_3O_4$/CuNCs/$ZnN_x$-PHNC. It could be observed that the metal nanoparticles were embedded in the graphitic carbon layer, inducing a polycrystalline structure, which improved the catalyst's stability. Further, measuring the lattice stripe spacing revealed that the 0.34 nm lattice spacing corresponded to the (002) crystalline plane of *C*. Compared with the standard $Fe_3O_4$ nanoparticle (PDF#76-0956), the 0.29 nm spacing corresponded to the (400) crystal plane of $Fe_3O_4$, while the 0.20 nm spacing was attributed to the (111) crystal plane (when compared with the standard Cu nanocluster, PDF#04-0836).[53] These results were consistent with those from the XRD analysis.

Additional elemental mapping images of $Fe_3O_4$/CuNCs/$ZnN_x$-PHNC using energy dispersive spectroscopy (EDS) (Fig. 1g) revealed that C, N, Fe, and Cu were uniformly dispersed on the skeletonized nanocages, and $Fe_3O_4$ nanoparticles were formed from the combination of Fe and O. The Cu nanoclusters were uniformly distributed in the nitrogen-doped carbon, forming $Fe_3O_4$ nanoparticles and Cu nanocluster active sites, which enabled efficient electron transfer during the ORR and enhanced the ORR catalytic activity.

### 3.2. Electrocatalytic performances of the catalysts

Next, cyclic voltammetry (CV) and linear scanning voltammetry (LSV) were performed to determine the electrocatalytic activity of the prepared catalysts for the ORR. The ORR performance of each catalyst was evaluated using commercial 20 wt% Pt/C. Fig. S7 (ESI†) shows the CV curves of the samples. In 0.1 M KOH electrolyte saturated with $N_2$, no obvious redox peak was observed for the four materials, indicating there were no other side reactions on the materials. Conversely, in the $O_2$-saturated electrolyte, oxygen-reduction peaks ensued, indicating oxygen electric reduction in the electrolyte. To investigate the ORR electrocatalytic activity of the synthesized catalyst materials, the catalytic performances of the materials were analyzed by testing the LSV curves with an electrochemical workstation.[54] From the LSV curves (Fig. 3a), we observed that $Fe_3O_4$/CuNCs/$ZnN_x$-PHNC outperformed the commercial 20 wt% Pt/C catalyst, with respective limiting currents of 5.69 and 5.63 mA $cm^{-2}$, indicating the enhanced conductivity of the $Fe_3O_4$/CuNCs/$ZnN_x$-PHNC catalyst for the ORR. The half-wave potential of $Fe_3O_4$/CuNCs/$ZnN_x$-PHNC was 0.832 V, better than the 0.814 V of 20 wt% Pt/C, indicating that $Fe_3O_4$/CuNCs/$ZnN_x$-PHNC reacted faster and had enhanced electrocatalytic activity. From the onset, $Fe_3O_4$/CuNCs/$ZnN_x$-PHNC evinced a superior half-wave potential and limiting current than those of $Fe_3O_4$/$ZnN_x$-PHNC, CuNCs/$ZnN_x$-PNC, and $ZnN_x$-PNC. Moreover, metal doping enhanced the conductivity and electron-donation ability of the material, proving that the abundant active sites of $Fe_3O_4$ nanoparticles and Cu nanogroups co-promoted the improved ORR activity.[55]

Meanwhile, the Tafel slope values of $Fe_3O_4$/CuNCs/$ZnN_x$-PHNC, $Fe_3O_4$/$ZnN_x$-PHNC, CuNCs/$ZnN_x$-PNC, $ZnN_x$-PNC, and Pt/C were obtained as 54, 43, 109, 66, and 88 mV $decade^{-1}$, respectively (Fig. 3b). The Tafel slopes of CuNCs/$ZnN_x$-PNC and $ZnN_x$-PNC were large, reflecting their poor ORR kinetic performance.[56] For the mono-metallic catalyst samples, the lack of active sites and PHNC structure led to their failure to achieve the expected ORR performance. $Fe_3O_4$/CuNCs/$ZnN_x$-PHNC and $Fe_3O_4$/$ZnN_x$-PHNC had lower Tafel slopes and higher reaction kinetics than Pt/C, indicating that the active site and hollow nanocage structure promoted the ORR activity. On the other hand, it also indicated that the nanocage structure was essential for enhancing electron transport and improving the reaction kinetics. Further, the ORR properties of $Fe_3O_4$/CuNCs/$ZnN_x$-PHNC and some recently published Fe-based catalysts were compared (Table S7, ESI†) and competitive ORR catalytic performance was demonstrated.

In addition, the *K–L* equation is essential for analyzing the ORR kinetics. As shown in Fig. S8 (ESI†), the *K–L* curves of the four materials displayed a good linear relationship, suggesting that their ORR reactions followed first-order kinetics. Meanwhile, the smaller the interval between the *K–L* curves, the more complete their ORR kinetics. The average numbers of transferred electrons for $Fe_3O_4$/CuNCs/$ZnN_x$-PHNC, $Fe_3O_4$/$ZnN_x$-PHNC, CuNCs/$ZnN_x$-PNC, and $ZnN_x$-PNC were 4.0, 3.6, 2.4, and 3.7, respectively. These values indicate that the reaction for $Fe_3O_4$/CuNCs/$ZnN_x$-PHNC followed the four-electron reaction pathway entirely, whereas the other three materials also had incomplete side reactions.[17]

To further explore the actual catalytic pathway of each catalyst in the ORR reaction, RRDE test materials can be used

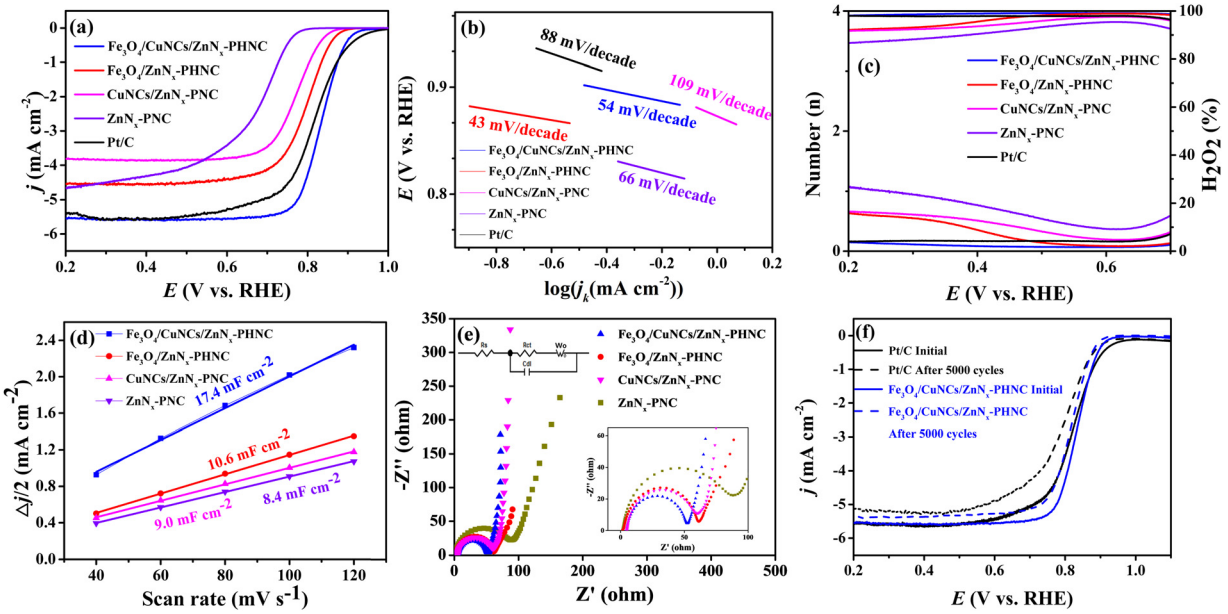


Fig. 3 (a) LSV curves for $Fe_3O_4$/CuNCs/$ZnN_x$-PHNC, $Fe_3O_4$/$ZnN_x$-PHNC, CuNCs/$ZnN_x$-PNC, $ZnN_x$-PNC and Pt/C; (b) Tafel curves; (c) hydrogen peroxide yield and average number of electrons transferred; (d) double-layer capacitance ($C_{dl}$); (e) impedance diagrams of $Fe_3O_4$/CuNCs/$ZnN_x$-PHNC, $Fe_3O_4$/$ZnN_x$-PHNC, CuNCs/$ZnN_x$-PNC and $ZnN_x$-PNC (insets show partial enlargements); (f) stability experiments of $Fe_3O_4$/CuNCs/$ZnN_x$-PHNC and Pt/C.

to calculate the respective electron-transfer number ($n$) and the corresponding hydrogen peroxide yield ($H_2O_2$%) according to the measured ring and disk currents. Fig. 3c illustrates that the electron-transfer numbers of $Fe_3O_4$/CuNCs/$ZnN_x$-PHNC and Pt/C were close to four, indicating that they were mainly involved in a four-electron transfer in the ORR reaction. Therefore, $H_2O_2$, as a product in the path of a two-electron reaction, was meager. At the same time, the electron-transfer numbers of $Fe_3O_4$/$ZnN_x$-PHNC, CuNCs/$ZnN_x$-PNC, and $ZnN_x$-PNC were between three and four, suggesting a large number of two-electron-transfer pathways in their ORR reactions, generating a large amount of $H_2O_2$, thereby resulting in a relatively poor ORR activity. Also, it indicates that the synergistic effect of bimetals reduced the $H_2O_2$ production rate and accelerated the four-electron-transfer process during the reaction.

The magnitude of the electrochemical double-layer capacitance ($C_{dl}$) of an electrode is related linearly to the active specific surface area of the catalyst, with a larger $C_{dl}$ resulting in a larger active specific surface area of the catalyst. The CV curves of $Fe_3O_4$/CuNCs/$ZnN_x$-PHNC were tested under various scan rates at 1.106–1.175 V (*vs.* RHE) (Fig. S9, ESI†). At different scan rates, half of the sum of the absolute values of the current densities of the cathode and anode at 1.15 V were taken, and the slopes obtained were plotted and fitted to the $C_{dl}$ of the electrodes of 17.4, 10.6, 9.0, and 8.4 mF $cm^{-2}$ (Fig. 3d). We noticed that the catalytic active sites significantly affected the double-layer capacitance of the catalyst. As the material underwent catalysis, PHNC increased the active specific surface area and the exposure of active sites, thus exhibiting higher catalysis.

Electrochemical impedance spectroscopy (EIS) was next performed focused on the electrical conductivity and charge-transfer kinetics of the electrodes. For the collection of the EIS spectrum, it was obtained at a potential of −0.15 V, amplitude of 0.005 V, and frequency of 0.005 Hz to 1000 Hz. Fig. 3e shows the EIS measurements of $Fe_3O_4$/CuNCs/$ZnN_x$-PHNC, $Fe_3O_4$/$ZnN_x$-PHNC, CuNCs/$ZnN_x$-PNC, and $ZnN_x$-PNC fitted to the simulated equivalent circuit diagram based on the shape of the curve. The curves had semicircular and linear parts, so the simulation yielded the main components of the circuit consisting of $R_s$, $R_{ct}$, $C_{dl}$, and $W_o$, where $R_s$ is the electrolyte internal resistance, which is the sum of the material's internal resistance and the contact resistance between the material and the electrolyte surface, while $R_{ct}$ is the charge-transfer resistance, expressed by the radius of the fitted semicircle. According to the fitted impedance values of the circuit diagram (Table S8, ESI†), $Fe_3O_4$/CuNCs/$ZnN_x$-PHNC had the least resistance and the fastest charge transfer during the charge and material transfers. The accelerated charge transfer could be attributed to the following: (1) the doping of $Fe_3O_4$ and Cu nanoparticles increased the material's conductivity; (2) the skeletonized nanocage structure accelerated $O_2$ diffusion, thereby shortening the electron-transport distance; (3) the graphitized carbon and abundant carbon defects after sintering further accelerated the electron transport.[57]

Methanol tolerance and stability are important indicators for evaluating the catalytic activity and reproducibility of materials. Fig. S10a–c (ESI†) show that the current of $Fe_3O_4$/CuNCs/$ZnN_x$-PHNC decreased by 2% after adding different molar concentrations of methanol, albeit the current normalized quickly. The curves of Pt/C further indicated that the current did not return to the original current after a 5% drop. Such a high tolerance and stability of $Fe_3O_4$/CuNCs/$ZnN_x$-PHNC was mainly attributed to the stable skeletonized nanocages and the increased graphitization. Fig. 3f shows the durability of $Fe_3O_4$/CuNCs/$ZnN_x$-PHNC and Pt/C. After 5000 CV cycles, the ultimate

current density decreased by 5% and 6.9% for $Fe_3O_4$/CuNCs/$ZnN_x$-PHNC and Pt/C, respectively. Accordingly, the onset electricity of $Fe_3O_4$/CuNCs/$ZnN_x$-PHNC and Pt/C decreased by 6 and 20 mV, respectively, and the half-wave potential depreciated by 8 and 24 mV, respectively. These values proved that the skeletonized nanocage structure and the degree of graphitization in $Fe_3O_4$/CuNCs/$ZnN_x$-PHNC were essential for enhancing the stability.[58]

### 3.3. Liquid and solid-state Zn–air battery performances of the catalysts

To verify the practical application of the material, we constructed a ZAB with a polished zinc plate as the anode and $Fe_3O_4$/CuNCs/$ZnN_x$-PHNC material-coated nickel foam as the cathode (Fig. 4a). The alkaline electrolyte was 6 M KOH + 0.2 M $Zn(CH_3COO)_2$. The $Fe_3O_4$/CuNCs/$ZnN_x$-PHNC assembled cell showed relatively strong stability. The inset in Fig. 4b depicts the actual test of the open-circuit voltage of the cell using a multimeter (OCV = 1.45 V). The multiplier performance of the battery was tested in the multi-current steps mode. Fig. S11 (ESI†) shows that the voltage changed at the beginning when various current densities were applied. However, the voltage was normal at the same current density, indicating that the material had excellent stability and multiplier performance.[59]

The power densities of the $Fe_3O_4$/CuNCs/$ZnN_x$-PHNC and Pt/C-based ZABs were 162 and 144 mW $cm^{-2}$, respectively (Fig. 4c). Comparing the power densities suggests that the $Fe_3O_4$/CuNCs/$ZnN_x$-PHNC-based assembled cells were significantly stronger than the Pt/C-based ones in terms of the discharge. The discrepancy could be ascribed to the superior ORR from the $Fe_3O_4$/CuNCs/$ZnN_x$-PHNC catalytic activity.[60] Fig. 4d illustrates the specific capacities of $Fe_3O_4$/CuNCs/$ZnN_x$-PHNC at 5, 10, and 15 mA $cm^{-2}$ as 818, 760, and 721 mA h $g^{-1}$, respectively. Comparing the specific capacities of $Fe_3O_4$/CuNCs/$ZnN_x$-PHNC and Pt/C at a 10 mA $cm^{-2}$ discharge density (Fig. 4e) showed that $Fe_3O_4$/CuNCs/$ZnN_x$-PHNC had superior ORR activity over Pt/C. Further, Fig. 4f depicts a 30 min discharge and 30 min charge cycle test for

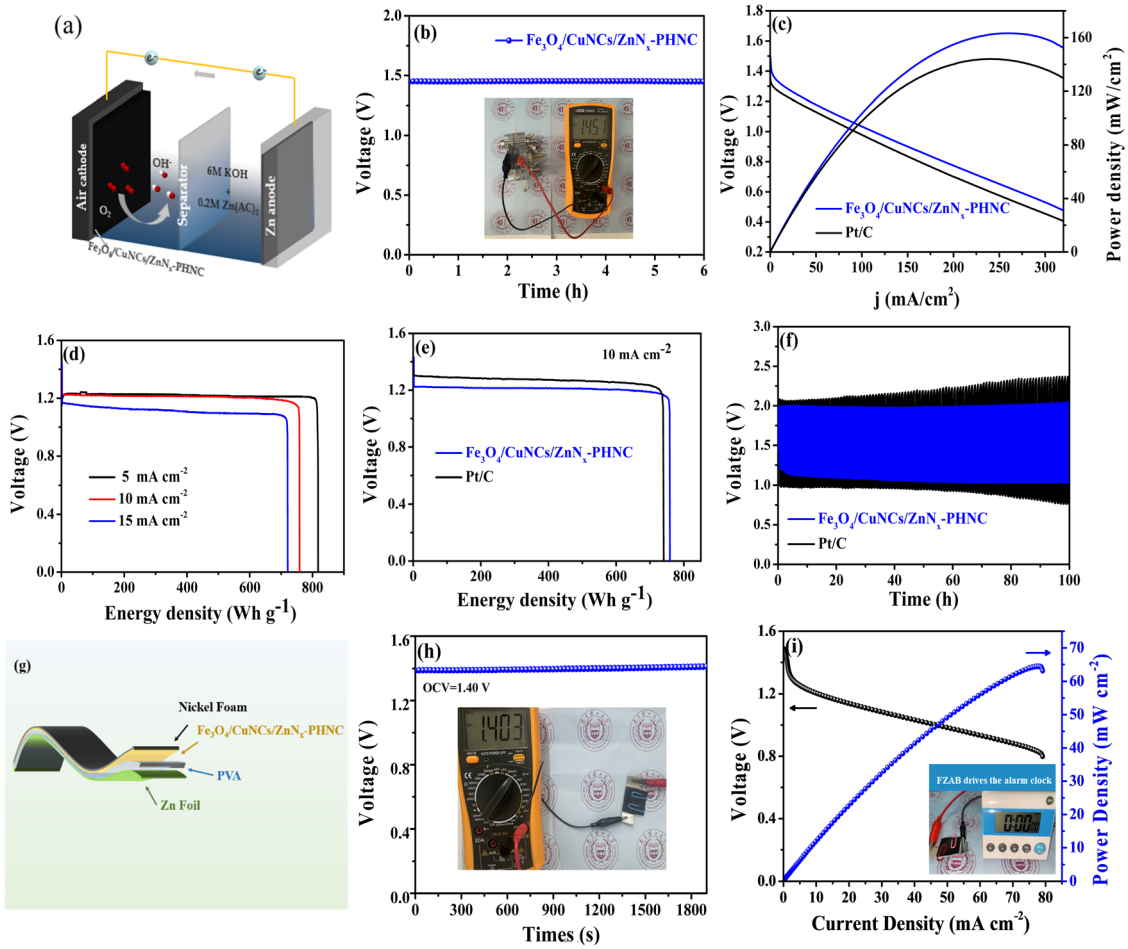


Fig. 4 (a) Schematic of the assembled ZAB; (b) open-circuit voltage of the $Fe_3O_4$/CuNCs/$ZnN_x$-PHNC-based ZAB (inset is the actual measurement using the universal meter). (c) Polarization curves and power density curves of $Fe_3O_4$/CuNCs/$ZnN_x$-PHNC and Pt/C-based ZABs. (d) Specific capacity curves of $Fe_3O_4$/CuNCs/$ZnN_x$-PHNC-based ZABs at different current densities. (e) Specific capacity curves of $Fe_3O_4$/CuNCs/$ZnN_x$-PHNC and Pt/C-based ZABs at a current density of 10 mA $cm^{-2}$. (f) Charge/discharge curves of $Fe_3O_4$/CuNCs/$ZnN_x$-PHNC and Pt/C-based ZABs at a current density of 10 mA $cm^{-2}$. (g) Schematic of a FZAB. (h) OCV plots (inset: multimeter measurement picture). (i) Polarization and power density curves (inset: FZAB powering an alarm clock).

$Fe_3O_4$/CuNCs/$ZnN_x$-PHNC and Pt/C-based catalyst cells at 10 mA $cm^{-2}$. After 100 h of cycling, the Pt/C-based ZAB showed an unstable charging and discharging voltage plateau, while $Fe_3O_4$/CuNCs/$ZnN_x$-PHNC maintained a stable charging and discharging voltage. Fig. S12a (ESI†) shows a stable charge/discharge plateau of the cell for 500 h at a current density of 5 mA $cm^{-2}$. A stable charge/discharge was also maintained at 15 mA $cm^{-2}$ for up to 200 h (Fig. S12b, ESI†). When the current density is too high, the durability of the battery will decrease, and the charging and discharging platforms will increase. Therefore, when the current density reached up to 20 mA $cm^{-2}$, the charge/discharge test was conducted for 10 min each, and the battery maintained an excellent plateau for 500 cycles (Fig. S12c, ESI†). The combined charge/discharge tests at various current densities revealed that the $Fe_3O_4$/CuNCs/$ZnN_x$-PHNC-based battery had excellent stability, mainly due to the skeletonized nanocage structure and abundant active sites of the material.[61] By comparing recent articles (Table S9, ESI†), the $Fe_3O_4$/CuNCs/$ZnN_x$-PHNC-based ZABs evinced a relatively impressive performance compared to that of other reported systems.

To further research into the potential of the rechargeable ZABs and their application in the increasingly attractive wearable electronic devices, we assembled FZABs and tested their performance. Among them, a 0.1 mm zinc plate was used as the anode, a PVA gel polymer as the electrolyte, and a nickel foam-loaded $Fe_3O_4$/CuNCs/$ZnN_x$-PHNC as the air cathode (Fig. 4g). After a long-time open-circuit voltage test, we observed that the open-circuit voltage of the assembled FZAB was stable at 1.40 V (Fig. 4h), as proven by the attached multimeter picture. Fig. 4i illustrates that it demonstrated an excellent peak power density of 64.5 mW $cm^{-2}$. To ascertain its practical usability, despite the adequate data support, we assembled a battery-driven LED electronic screen alarm clock. Here, we found that it could be used seamlessly, showing its future commercial prospects and practical applicability (video 1, ESI†).

## 4. Conclusions

A heterogeneous skeletonized nanocage catalyst $Fe_3O_4$/CuNCs/$ZnN_x$-PHNC loaded with bimetals was prepared by stirring at room temperature and annealing at high temperature with NaCl and KCl as protectants and stripping agents, respectively. The rich active sites produced by the synergistic action of various metals and hollow nanostructures enabled the catalysts to show excellent ORR performance. When the prepared materials were used as liquid ZAB cathode catalysts, the ZABs exhibited excellent performance with a high OCV (1.45 V) and peak power density (162 mW $cm^{-2}$). In addition, the ultrahigh specific capacity (760 mA h $g^{-2}$) at a 10 mA $cm^{-2}$ current density was far superior to that of the benchmark Pt/C-based catalyst. In addition, the $Fe_3O_4$/CuNCs/$ZnN_x$-PHNC-based ZAB could be charged and discharged for more than 500 h at a 5 mA $cm^{-2}$ current density, thus demonstrating high stability and high cycling performance. The excellent performance of the assembled FAZBs also proved their practical application potential as wearable flexible batteries. Overall, this study provides a feasible way to prepare efficient catalysts for ZAB cathodes to replace noble metal catalysts in practical applications.

## Data availability

The data supporting this article have been included as part of the ESI,† and in the Experimental section of the manuscript.

## Conflicts of interest

The authors declare no competing financial interest.

## Acknowledgements

The Jiangsu Provincial Key Research and Development Program (BE2023820, BE2021720), Qinglan Project of Jiangsu Province of China, State Key Laboratory of Pollution Control and Resource Reuse Foundation (PCRRF19032) are greatly acknowledged.

## References

1 Y. Jiao, X. Gu, P. Zhai, Y. Wei, W. Liu, Q. Chen, Z. Yang, J. Zuo, L. Wang, T. Xu and Y. Gong, *Nano Lett.*, 2022, **22**, 7386–7393.
2 N. Shang, K. Wang, M. Wei, Y. Zuo, P. Zhang, H. Wang, Z. Chen and P. Pei, *J. Mater. Chem. A*, 2022, **10**, 16369–16389.
3 M. Katsaiti, E. Papadogiannis, V. Dracopoulos, A. Keramidas and P. Lianos, *J. Power Sources*, 2023, **555**, 232384.
4 A. Wang, X. Zhang, S. Gao, C. Zhao, S. Kuang, S. Lu, J. Niu, G. Wang, W. Li, D. Chen, H. Zhang, X. Zhou, S. Zhang, B. Zhang and W. Wang, *Adv. Mater.*, 2022, **n/a**, 2204247.
5 X. Chen, J. Pu, X. Hu, Y. Yao, Y. Dou, J. Jiang and W. Zhang, *Small*, 2022, **18**, 2200578.
6 W. Zhu, H. Liu, R. Yue, Y. Pei, J. Zhang, X. Liu, R. Li, Y. Yin and M. D. Guiver, *Small*, 2022, **18**, 2202660.
7 Y. Rao, W. Li, S. Chen, Q. Yue, Y. Zhang and Y. Kang, *Small*, 2022, **18**, 2104411.
8 A. Yu, Z. Peng, Y. Li, L. Zhu, P. Peng and F.-F. Li, *ACS Appl. Mater. Interfaces*, 2022, **14**, 42337–42346.
9 S. Huang, H. Zhang, J. Zhuang, M. Zhou, M. Gao, F. Zhang and Q. Wang, *Adv. Energy Mater.*, 2022, **12**, 2103622.
10 S. Wu, D. Deng, E. Zhang, H. Li and L. Xu, *Carbon*, 2022, **196**, 347–353.
11 L. Xu, S. Wu, X. He, H. Wang, D. Deng, J. Wu and H. Li, *Chem. Eng. J.*, 2022, **437**, 135291.
12 D. Deng, H. Ma, S. Wu, H. Wang, J. Qian, J. Wu, H. Li, C. Yan, H. Li and L. Xu, *Renewables*, 2023, **1**, 362–372.
13 Y. Sun, X. Liu, M. Zhu, Z. Zhang, Z. Chen, S. Wang, Z. Ji, H. Yang and X. Wang, *DeCarbon*, 2023, **2**, 100018.
14 H. Liu, F. Yu, K. Wu, G. Xu, C. Wu, H.-K. Liu and S.-X. Dou, *Small*, 2022, **18**, 2106635.
15 H. Yang, H. Huang, Q. Wang, L. Shang, T. Zhang and S. Wang, *J. Mater. Chem. A*, 2023, **11**, 6191–6197.
16 D. Deng, J. Qian, X. Liu, H. Li, D. Su, H. Li, H. Li and L. Xu, *Adv. Funct. Mater.*, 2022, **32**, 2203471.

17 W. Li, J. Wang, J. Chen, K. Chen, Z. Wen and A. Huang, *Small*, 2022, **18**, 2202018.
18 Y. Arafat, M. R. Azhar, Y. Zhong, H. R. Abid, M. O. Tadé and Z. Shao, *Adv. Energy Mater.*, 2021, **11**, 2100514.
19 Q. Yu, J. Lv, J. Li, R. Yu, J. Wu, S. Xi, X. Li, N. Xu, L. Zhou and L. Mai, *Energy Environ. Mater.*, 2023, **6**, e12389.
20 Y. Pan, Q. Yang, F. Qiu, X. Liu, C. Shen, Y. Fan, H. Song and S. Zhang, *Mater. Today Chem.*, 2023, **34**, 101787.
21 Y. Pan, X. Ma, M. Wang, X. Yang, S. Liu, H.-C. Chen, Z. Zhuang, Y. Zhang, W.-C. Cheong, C. Zhang, X. Cao, R. Shen, Q. Xu, W. Zhu, Y. Liu, X. Wang, X. Zhang, W. Yan, J. Li, H. M. Chen, C. Chen and Y. Li, *Adv. Mater.*, 2022, **34**, 2203621.
22 L. Deng, L. Qiu, R. Hu, L. Yao, Z. Zheng, X. Ren, Y. Li and C. He, *Appl. Catal., B*, 2022, **305**, 121058.
23 W. Wang, Q. Jia, S. Mukerjee and S. Chen, *ACS Catal.*, 2019, **9**, 10126–10141.
24 T. Sun, S. Mitchell, J. Li, P. Lyu, X. Wu, J. Perez-Ramirez and J. Lu, *Adv. Mater.*, 2021, **33**, e2003075.
25 Y. Cheng, M. Wang, S. Lu, C. Tang, X. Wu, J.-P. Veder, B. Johannessen, L. Thomsen, J. Zhang, S.-Z. Yang, S. Wang and S. P. Jiang, *Appl. Catal., B*, 2021, **284**, 119717.
26 Y. Shen, Y. Xiao, H. Zhang, H. Fan, Y. Li, Z. Yan and W.-H. Zhang, *Chem. Eng. J.*, 2023, **477**, 146823.
27 M. Tong, F. Sun, Y. Xie, Y. Wang, Y. Yang, C. Tian, L. Wang and H. Fu, *Angew. Chem., Int. Ed.*, 2021, **60**, 14005–14012.
28 G. Yang, P. Hu, Y. Cao, F. Yuan and R. Xu, *Nanoscale Res. Lett.*, 2010, **5**, 1437.
29 Y. Liu, H. Jiang, J. Hao, Y. Liu, H. Shen, W. Li and J. Li, *ACS Appl. Mater. Interfaces*, 2017, **9**, 31841–31852.
30 H. Hu, B. Guan, B. Xia and X. W. Lou, *J. Am. Chem. Soc.*, 2015, **137**, 5590–5595.
31 K. Ding, J. Hu, J. Luo, L. Zhao, W. Jin, Y. Liu, Z. Wu, G. Zou, H. Hou and X. Ji, *Adv. Funct. Mater.*, 2022, **n/a**, 2207331.
32 A. R. C. Bredar, M. D. Blanchet, A. R. Burton, B. E. Matthews, S. R. Spurgeon, R. B. Comes and B. H. Farnum, *ACS Catal.*, 2022, **12**, 3577–3588.
33 W. da Silva Freitas, A. D'Epifanio, C. Lo Vecchio, I. Gatto, V. Baglio, V. C. A. Ficca, E. Placidi and B. Mecheri, *Chem. Eng. J.*, 2023, **465**, 142987.
34 C. Xuan, B. Hou, W. Xia, Z. Peng, T. Shen, H. L. Xin, G. Zhang and D. Wang, *J. Mater. Chem. A*, 2018, **6**, 10731–10739.
35 W. Wang, J. Si, J. Li, Q. Wang and S. Chen, *Int. J. Hydrogen Energy*, 2016, **41**, 16858–16864.
36 Q. Lv, N. Wang, W. Si, Z. Hou, X. Li, X. Wang, F. Zhao, Z. Yang, Y. Zhang and C. Huang, *Appl. Catal., B*, 2020, **261**, 118234.
37 K. Yang, Y. Cheng, Y. Lei, Q. Yang, X. Liu, T. Lu, H. Xie, J. Li, T. Zan and H. Wang, *J. Solid State Chem.*, 2024, **329**, 124401.
38 K. Sheng, Q. Yi, L. Hou and A. Chen, *J. Electrochem. Soc.*, 2020, **167**, 070560.
39 J. Gao, Y. Wang, H. Wu, X. Liu, L. Wang, Q. Yu, A. Li, H. Wang, C. Song, Z. Gao, M. Peng, M. Zhang, N. Ma, J. Wang, W. Zhou, G. Wang, Z. Yin and D. Ma, *Angew. Chem., Int. Ed.*, 2019, **58**, 15089–15097.
40 J. Zemek, J. Houdkova, P. Jiricek and M. Jelinek, *Carbon*, 2018, **134**, 71–79.
41 Y. Yang, X. Xu, P. Sun, H. Xu, L. Yang, X. Zeng, Y. Huang, S. Wang and D. Cao, *Nano Energy*, 2022, **100**, 107466.
42 C. Chen, J. Long, K. Shen, X. Liu and W. Zhang, *ACS Appl. Mater. Interfaces*, 2022, **14**, 38677–38688.
43 Y. Zuo, G. Wang, J. Peng, G. Li, Y. Ma, F. Yu, B. Dai, X. Guo and C.-P. Wong, *J. Mater. Chem. A*, 2016, **4**, 2453–2460.
44 Y. Li, Y. Fu, S. Chen, Z. Huang, L. Wang and Y. Song, *Composites, Part B*, 2019, **171**, 130–137.
45 P. Sarkar, N. Nandi, N. Barnwal and K. Sahu, *Mater. Today Chem.*, 2023, **27**, 101341.
46 Q. Wang, T. Ina, W.-T. Chen, L. Shang, F. Sun, S. Wei, D. Sun-Waterhouse, S. G. Telfer, T. Zhang and G. I. N. Waterhouse, *Sci. Bull.*, 2020, **65**, 1743–1751.
47 J. Xu, S. Lai, D. Qi, M. Hu, X. Peng, Y. Liu, W. Liu, G. Hu, H. Xu, F. Li, C. Li, J. He, L. Zhuo, J. Sun, Y. Qiu, S. Zhang, J. Luo and X. Liu, *Nano Res.*, 2020, **14**, 1374–1381.
48 Q. Yang, R. Liu, Y. Pan, Z. Cao, Y. Liu, L. Wang, J. Yu, H. Song, Z. Ye and S. Zhang, *J. Colloid Interface Sci.*, 2022, **628**, 691–700.
49 H. Yin, H. Xia, S. Zhao, K. Li, J. Zhang and S. Mu, *Energy Environ. Mater.*, 2021, **4**, 5–18.
50 Y. Chen, S. Ji, S. Zhao, W. Chen, J. Dong, W.-C. Cheong, R. Shen, X. Wen, L. Zheng, A. I. Rykov, S. Cai, H. Tang, Z. Zhuang, C. Chen, Q. Peng, D. Wang and Y. Li, *Nat. Commun.*, 2018, **9**, 5422.
51 K. Yu, K. Sun, W. C. Cheong, X. Tan, C. He, J. Zhang, J. Li and C. Chen, *Small*, 2023, **19**, 2302611.
52 B. Eren, D. Zherebetskyy, L. L. Patera, C. H. Wu, H. Bluhm, C. Africh, L.-W. Wang, G. A. Somorjai and M. Salmeron, *Science*, 2016, **351**, 475–478.
53 Y. Song, T. Zhang, G. Zhou, P. Liu, X. Yan, B. Xu and J. Guo, *Appl. Surf. Sci.*, 2022, **589**, 153022.
54 K. Yuan, S. Sfaelou, M. Qiu, D. Lützenkirchen-Hecht, X. Zhuang, Y. Chen, C. Yuan, X. Feng and U. Scherf, *ACS Energy Lett.*, 2018, **3**, 252–260.
55 J. Zhang, J. Chen, Y. Luo, Y. Chen, Y. Luo, C. Zhang, Y. Xue, H. Liu, G. Wang and R. Wang, *J. Mater. Chem. A*, 2021, **9**, 5556–5565.
56 J. H. Lee, J.-h Jang, J. Kim and S. J. Yoo, *J. Ind. Eng. Chem.*, 2021, **97**, 466–475.
57 Q. Yang, R. Liu, Y. Pan, Z. Cao, J. Zuo, F. Qiu, J. Yu, H. Song, Z. Ye and S. Zhang, *ACS Appl. Mater. Interfaces*, 2023, **15**, 5720–5731.
58 L. Li, Y. Li, Y. Xiao, R. Zeng, X. Tang, W. Yang, J. Huang, K. Yuan and Y. Chen, *Chem. Commun.*, 2019, **55**, 7538–7541.
59 Q. Yang, R. Liu, J. Gao, Y. Liu, S. Hu, H. Song and S. Zhang, *ACS Appl. Energy Mater.*, 2022, **5**, 1041–1051.
60 H. Jiang, J. Gu, X. Zheng, M. Liu, X. Qiu, L. Wang, W. Li, Z. Chen, X. Ji and J. Li, *Energy Environ. Sci.*, 2019, **12**, 322–333.
61 Y. Li, H. Huang, S. Chen, X. Yu, C. Wang and T. Ma, *Nano Res.*, 2019, **12**, 2774–2780.